

Misoriented Lamellar Microstructures in Mo-Si-Ti Alloy Due to Asymmetrical Nucleation Distance and Interfacial Energies: A Phase-Field Analysis

Yuhan Cai, Fei Wang,* and Britta Nestler

The material properties are crucially affected by the microstructure formed during solidification, which is typically divided into three stages: (I) Early stage of nucleation in molecule scale, which is beyond the scope of the mean-field model; (II) Middle stage of nucleation, where the dispersed nuclei have formed; (III) Late stage of nucleation, where the nuclei contact with each other. In previous studies, the formation of the stable eutectic lamellae is mostly based on the assumption that a stable solid–solid interface has already been established, corresponding to the stage (III), and the growth stage (II) is often overlooked. In the current work, by varying the nucleation density and distance, an alternative mechanism for the misoriented microstructure formation in Mo-Si-Ti alloy is proposed, which considers nucleation stage (II). Furthermore, the misorientation angle as a function of the nucleation density, distance, and the interfacial energies is quantified by systematic phase-field simulations. The simulated composition distribution reveals the mechanism for the misorientation of eutectic lamellar pairs, which becomes more pronounced when the solids-fluid interfacial energies are unequal. It is expected that the present work provides a potential perspective for the fundamental understanding of misoriented microstructures in solidification.

1. Introduction

Mo-Si-Ti alloys with eutectic microstructures, consisting of $\text{Ti}(\text{Mo})_5\text{Si}_3$ and $\beta(\text{Mo}, \text{Si}, \text{Ti})$, hold significant enhancement in material properties and exhibit outstanding performance, especially in oxidation and creep behavior.^[1–4] The inherent microstructural stability of eutectic phases contributes to enhanced thermal and mechanical reliabilities in harsh environments. This microstructural stability expands the potential applications of Mo-Si-Ti alloys in aerospace, energy production, and other industries requiring materials that can withstand extreme conditions. In experimental and numerical studies, it is often observed that some lamellar pairs show an unexpected bending/tilted growth during solidification process. Parisi et al.^[5] summarized three distinct types of eutectic instabilities: lamellar elimination, tilt instability, and oscillatory instability. The tilt instability may be caused by a symmetry breaking, which


could be engendered by several reasons, such as nucleation, noise, etc. Investigating the underlying mechanism of tilt instability using traditional experiments faces the following challenges: 1) Controlling all relevant parameters with high precision is difficult. 2) The tilted growth of eutectic alloy involves intricate interactions between multiple phases, making it challenging to isolate and study individual mechanisms. 3) Lamellar growth is a dynamic process, which is arduous to be captured in situ. 4) Understanding the role of interfaces in tilted growth requires detailed analysis of solid-solid and solid-liquid interfacial energies, which are open questions. However, it is of great feasibility to shed light on the growth of the $\text{Ti}(\text{Mo})_5\text{Si}_3$ and $\beta(\text{Mo}, \text{Si}, \text{Ti})$ lamellae by making effort of computational materials simulation methods.

Based on the experiments of organic alloy solidification, Podolinsky et al.^[6] proposed a stepwise eutectic formation mechanism. Initially, two different phases nucleate independently in the melt, and then the eutectic structures form of neighboring nuclei contacting each other. By this way, the nucleation process is likely classified into three stages: 1) Early stage of nucleation, where atoms, ions, or polymers accumulate to form the initial nuclei. 2) Middle stage of nucleation, characterized by nuclei of different phases forming and growing independently in the melt. 3) Late stage of nucleation, where solid-solid interfaces

Y. Cai, F. Wang, B. Nestler
Institute of Applied Materials-Microstructure Modelling and Simulation
Karlsruhe Institute of Technology (KIT)
Straße am Forum 7, 76131 Karlsruhe, Germany
E-mail: fei.wang@kit.edu

F. Wang, B. Nestler
Institute of Nanotechnology
Karlsruhe Institute of Technology (KIT)
Hermann-von-Helmholtz-Platz 1, 76344 Eggenstein-Leopoldshafen,
Germany

B. Nestler
Institute of Digital Materials Science
Karlsruhe University of Applied Sciences
Moltkestraße 30, 76133 Karlsruhe, Germany

 The ORCID identification number(s) for the author(s) of this article can be found under <https://doi.org/10.1002/adem.202302082>.

© 2024 The Authors. Advanced Engineering Materials published by Wiley-VCH GmbH. This is an open access article under the terms of the Creative Commons Attribution License, which permits use, distribution and reproduction in any medium, provided the original work is properly cited.

DOI: 10.1002/adem.202302082

between nuclei have been established and grow steadily with time. The first stage of nucleation relies on the consideration on molecular scale, such as molecular dynamics (MD) method,^[7,8] which is beyond the scope of the present mean-field model. Subsequent to this initial stage, the growth of the nuclei can be explored by using numerical methods at the mesoscopic scale, such as the phase-field method. The phase-field method has been proven to be a powerful technique to simulate the growth of intermetallic compounds in many alloys, e.g., Sn-Cu,^[9] Al-Ni,^[10] Mg-Al,^[11] Bi-In-Sn,^[12] Ni-Al-Cr-Mo,^[13] Fe-C.^[14] In the phase-field simulation studies, the tilted growth of the lamellar pair during eutectic transformation is explored by considering the influence of various factors. Mo et al.^[15] investigated the effect of solid–solid and solid–liquid interface anisotropy on the evolution of the tilted eutectic structure. Similarly, Lahiri et al.^[16] also considered the influence of the interfacial anisotropy on the morphology of eutectic solidification and observed tilted lamellae in 2D simulations as well as existence of the eutectic spirals in 3D simulations. Zhang et al.^[17] studied the lamellar eutectic growth under the effect of forced convection in melt. A horizontal external force induced a flow resulting in a tilted eutectic lamellar front by altering the solute distribution near the interface; similar tilted phase growths are observed for grain boundary^[18] and dendrite^[19] with external lateral flow. Noubary et al.^[20] investigated the effect of different parameters, such as interfacial energies, diffusion coefficients, lamellar spacing, and solidification velocity, on the ternary eutectics morphology in an idealized system. They observed that the tilted growth of the eutectics occurs for special ratios of interfacial energies between solid/solid and solid/liquid phases. Nevertheless, the studies mentioned above primarily concentrate on the morphological evolution of eutectic lamellae after forming the solid-solid interface (late stage of nucleation). Consequently, the impact from the nucleation randomness in middle stage has not been accounted for.

As nucleation can only be statistically analyzed in experiments and significant differences exist among experimental data, as summarized in **Table 1**, we address this gap by meticulously scrutinizing the morphological evolution of eutectic lamellae depending on the nucleation characteristics. This is achieved through precise control of the nucleation distance ratio between two solid particles by utilizing phase-field simulations. Moreover, the understanding of the influence of combined effect between

Table 1. Summarizing the nucleation density for different systems under distinct solidification/condensation conditions.

Material ^{a)}	Surrounding matrix	Year	Nucleation density [m ⁻³]
ω Ti-Mo alloy	β-type Ti-Mo alloys	2011	8 × 10 ²¹ [40]
Al crystal	Al ₈₈ Y ₇ Fe ₅	1999	3 × 10 ²¹ [41]
	Al ₉₀ Gd ₅ Fe ₅	1991	6 × 10 ²¹ [42]
	Al ₉₂ Sm ₈	1998	5 × 10 ²¹ –4 × 10 ²¹ [43,44]
β-Al ₅ FeSi intermetallics	Al-7.5Si-3.5Cu-0.6Fe	2014	3 × 10 ¹⁰ [45]
Water droplet	Air	2014	6.5 × 10 ¹² –1.3 × 10 ¹⁴ [46,47]
	Air	2020	1.2 × 10 ¹⁴ –8 × 10 ¹⁸ [48]

^{a)}All experimental data are transformed to the particles per unit volume (m⁻³).

the interfacial energy and nucleation on the solidification morphology, especially from experimental studies, is considerably limited, since an accurate measurement of the interfacial energy and a precise control of the nucleation both are almost impossible in experiments. The role of this combined effect will be studied in the present work by simulations.

In particular, we cast light on the lamellae growth during a eutectic transformation in Mo-Si-Ti alloy. By using phase-field method, we investigate the evolution of lamellar pairs Ti(Mo)₅Si₃ and β(Mo, Si, Ti) under various nucleation distance ratios and with different nucleation densities. Through the analysis of concentration variations at the triple points L/TS/β on both sides of β phase, we elucidate the underlying mechanism behind the three observed growth modes in simulations: (g_i) stable, (g_{ii}) regular tilted, and (g_{iii}) irregular growth modes, and identify growth type diagrams. Furthermore, we examine the morphological evolution of the eutectic lamellae under the combined effect of disparate interfacial energy and unequal nucleation distances. Additional experimental conditions, such as temperature gradient as well as other solidification conditions that are difficult to be controlled in experiments, for example, the radius and shape of the initial nuclei, will be explored in a separate forthcoming study.

2. Phase-Field Model

In the present work, a thermodynamically consistent phase-field model based on a grand potential functional is applied to study the three-phase eutectic transformation, L → Ti(Mo)₅Si₃ + β(Mo, Si, Ti), in Mo-Si-Ti ternary alloy.^[21,22] An order parameter φ_α is used to represent the local volume fraction of each phase α . The value of φ_α characterizes the phase state of the system with respect to phase α temporally and spatially. In particular, the phase-field vector $\boldsymbol{\varphi} = (\varphi_1, \dots, \varphi_N)$ is applied to designate the phase state of the system with N phases. For the mass conservation of multiple components K , we introduce respective diffusion equations for K components c_i ($i = 1, \dots, K$), which follow the Fick's law and which are related to K chemical potentials μ_i ($i = 1, \dots, K$). The coupling of the N phase-fields with K chemical potentials results in the following set of evolution equations:

$$\tau_{\alpha\beta}\varepsilon \frac{\partial \varphi_\alpha}{\partial t} = \varepsilon \underbrace{\left[\frac{\partial a(\boldsymbol{\varphi}, \nabla \boldsymbol{\varphi})}{\partial \varphi_\alpha} - \nabla \cdot \frac{\partial a(\boldsymbol{\varphi}, \nabla \boldsymbol{\varphi})}{\partial \nabla \varphi_\alpha} \right]}_{=: rhs_\alpha} - \frac{1}{\varepsilon} \frac{\partial w(\boldsymbol{\varphi})}{\partial \varphi_\alpha} - \frac{\partial \Psi(\boldsymbol{\varphi}, \boldsymbol{\mu})}{\partial \varphi_\alpha} - \Lambda$$

$$\alpha = 1, \dots, N, \beta \neq \alpha \quad (1)$$

$$\frac{\partial \boldsymbol{\mu}}{\partial t} = \left[\sum_{\alpha=1}^N \frac{\partial c^\alpha(\boldsymbol{\mu})}{\partial \boldsymbol{\mu}} k(\varphi_\alpha) \right]^{-1} \cdot \left[(\nabla \cdot (\mathbf{M}(\boldsymbol{\varphi}, \boldsymbol{\mu}) \nabla \boldsymbol{\mu}) - \mathbf{J}_{at}) \right]$$

$$- \sum_{\alpha=1}^N c^\alpha(\boldsymbol{\mu}) k'(\varphi_\alpha) \frac{\partial \varphi_\alpha}{\partial t} \quad (2)$$

The Lagrange multiplier Λ in Equation (1) is defined as

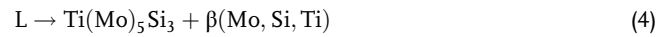
$$\Lambda = \frac{1}{N} \sum_{\alpha=1}^N rhs_\alpha \quad (3)$$

to ensure the constraint: $\sum_{\alpha=1}^N \varphi_{\alpha} = 1$. The modeling parameter $\tau_{\alpha\beta}$ is a relaxation constant at the α/β interface and calculated by relating the driving force of the difference in the grand chemical potential with the undercooling.^[23] The profile of the diffuse interface between the phases is modeled by the gradient energy term $a(\varphi, \nabla\varphi)$ and the obstacle potential term $w(\varphi)$; the length parameter ε controls the interface width. Based on Equation (1), the interface width is derived as $\Gamma = \varepsilon\pi^2/4$ in 1D case for equilibrium solidification by considering $\Delta\Psi = \Psi^{\alpha} - \Psi^{\beta} = 0$. In order to determine the parameter ε , we compare the interfacial profile φ_{β} from our simulation with the theoretical calculation. Likewise, φ_{β} is also derived from Equation (1) and written as $\varphi(x) = 0.5 + 0.5 \sin(4x/\varepsilon\pi)$. A suitable ε is chosen by considering the following two factors: an acceptable deviation of the simulation results for the interfacial profile from theoretical calculation, and the reduction of computational effort. For a detailed selection process of the interface width, we refer to our previous papers.^[14,24] The driving force for the phase transition is described by the difference in the grand chemical potentials Ψ , which are calculated from the material-specific Gibbs free energies. The Gibbs free energies of the Mo-Si-Ti system are incorporated from the thermodynamic Calphad database^[25] to ensure the thermodynamic consistency of the model. The concentration vector is written as $\mathbf{c}^{\alpha} = (c_1^{\alpha}, \dots, c_K^{\alpha})$ and the chemical potential vector is defined as $\boldsymbol{\mu} = (\mu_1, \dots, \mu_K)$. The evolution equation of the chemical potentials is given by Equation (2), with the mobility term \mathbf{M} , the anti-trapping current \mathbf{J}_{at} ,^[22,26] and an interpolation function $k(\varphi_{\alpha}) = \varphi_{\alpha}^2(3 - 2\varphi_{\alpha})$.^[27,28] We refer to refs. [22,24] for the details of the derivation of this phase-field model. To use the approach for solidification in Mo-Si-Ti, the parameters and quantities of the various terms are configured accordingly. The simulation parameters are tabulated in **Table 2**. It should be noted that the self-diffusion coefficients of molybdenum and tantalum in the melt are related to their melting points.^[29] We assume that the self-diffusion coefficients of titanium and silicon have similar dependence on T and are calculated accordingly. In this study, the interdiffusivities of the three considered components in the melt are calculated using Darken's equation.^[30,31] For more complex systems, other methods, such as the Matano-based approach,^[32,33] need to be applied to quantify the interdiffusion coefficients. Based on the self-diffusion of titanium D_{Ti}^{S} and impurity diffusion coefficients

of molybdenum D_{Mo}^{L} in β -Ti matrix with body-centered cubic structure from,^[34] the diffusion coefficients of titanium and molybdenum in the solid phases are considerably lower than those in the liquid phase at the considered temperature of 1913 K. Consequently, we omit the diffusion in the solid phases for simplification. Due to the significant difficulty in measuring interfacial energy in experiments, obtaining its absolute value requires complex calculation.^[35–37] For simplicity, we assume identical interfacial energies of liquid-Ti(Mo)₅Si₃ and β (Mo, Si, Ti)-Ti(Mo)₅Si₃ to study their influence on the final solidified morphology. Generally, interfacial energies are essentially a function of concentration. However, describing the dependence of interfacial energy on concentration remains an open question and will not be discussed in this work.

3. Phase Diagram of Mo-Si-Ti

To investigate the phase transformation of a solidification process caused by an undercooled melt, we consider temperature-dependent free energy functions of each phase in the phase-field model. In the current work, we focus on the three-phase eutectic reaction



in the temperature range from 1893 to 1923 K. The free energy density of the liquid phase is expressed via a parabolic form^[24,38]

$$f^{\text{L}} = a(T)^{\text{L}}c_{\text{Mo}}^{\text{L}}c_{\text{Mo}}^{\text{L}} + b(T)^{\text{L}}c_{\text{Mo}}^{\text{L}} + d(T)^{\text{L}} + e(T)^{\text{L}}c_{\text{Ti}}^{\text{L}}c_{\text{Ti}}^{\text{L}} + g(T)^{\text{L}}c_{\text{Ti}}^{\text{L}} + h(T)^{\text{L}}c_{\text{Mo}}^{\text{L}}c_{\text{Ti}}^{\text{L}} \quad (5)$$

and fitted by the least square method based on the thermodynamic data^[25] at the temperature 1893, 1898, 1903, 1913, 1918, and 1923 K, respectively. The coefficients a, b, d, e, g, h are temperature dependent. **Figure 1** illustrates the free energy density of the liquid phase as a function of c_{Mo} for these four exemplary temperatures; fitting curves and CALPHAD data are represented by the solid line and circular symbols, respectively. In CALPHAD database, the intermetallic phase Ti(Mo)₅Si₃ is exactly stoichiometric with a constant Si concentration 0.375 and the solubility of the silicon in the β phase varies slightly between 0 and 0.07 in the considered temperature range. In the following sections, we use the notations TS and β to represent Ti(Mo)₅Si₃ and β (Mo, Si, Ti) phase, respectively. Due to the limited thermodynamic data of TS and β phases, we assume that the free energy functions of these two phases are formulated as

$$f^{\text{TS}} = \left[a(T)^{\text{TS}}(c_{\text{Mo}}^{\text{TS}} + b(T)^{\text{TS}})^2 + d(T)^{\text{TS}} \right] + n^{\text{TS}}(0.625 - c_{\text{Mo}}^{\text{TS}} - c_{\text{Ti}}^{\text{TS}})^2 \quad (6)$$

and

$$f^{\beta} = \left[a(T)^{\beta}(c_{\text{Mo}}^{\beta} + b(T)^{\beta})^2 + d(T)^{\beta} \right] + n^{\beta}(0.963 - c_{\text{Mo}}^{\beta} - c_{\text{Ti}}^{\beta})^2 \quad (7)$$

We refer to ref. [24] for a detailed explanation and reasonability of this assumption. The free energy densities of TS and β are

Table 2. Parameters for the phase-field simulations.

Symbol	Description	Value
Δt	Time step	1×10^{-7} s
Δx	Space step	1×10^{-8} m
$\sigma_{\text{L/T}}$	Interfacial energy between liquid and Ti(Mo) ₅ Si ₃ phases	0.5 Jm^{-2}
$\sigma_{\text{T}/\beta}$	Interfacial energy between Ti(Mo) ₅ Si ₃ and β (Mo, Si, Ti) phases	0.5 Jm^{-2}
D_{Mo}^{L}	Self-diffusion coefficient of Mo in the liquid phase	$4.2 \times 10^{-9} \text{ m}^2 \text{ s}^{-1}$ ^[29]
D_{Ti}^{L}	Self-diffusion coefficient of Ti in the liquid phase	$4.2 \times 10^{-9} \text{ m}^2 \text{ s}^{-1}$
D_{Si}^{L}	Self-diffusion coefficient of Si in the liquid phase	$4.2 \times 10^{-9} \text{ m}^2 \text{ s}^{-1}$

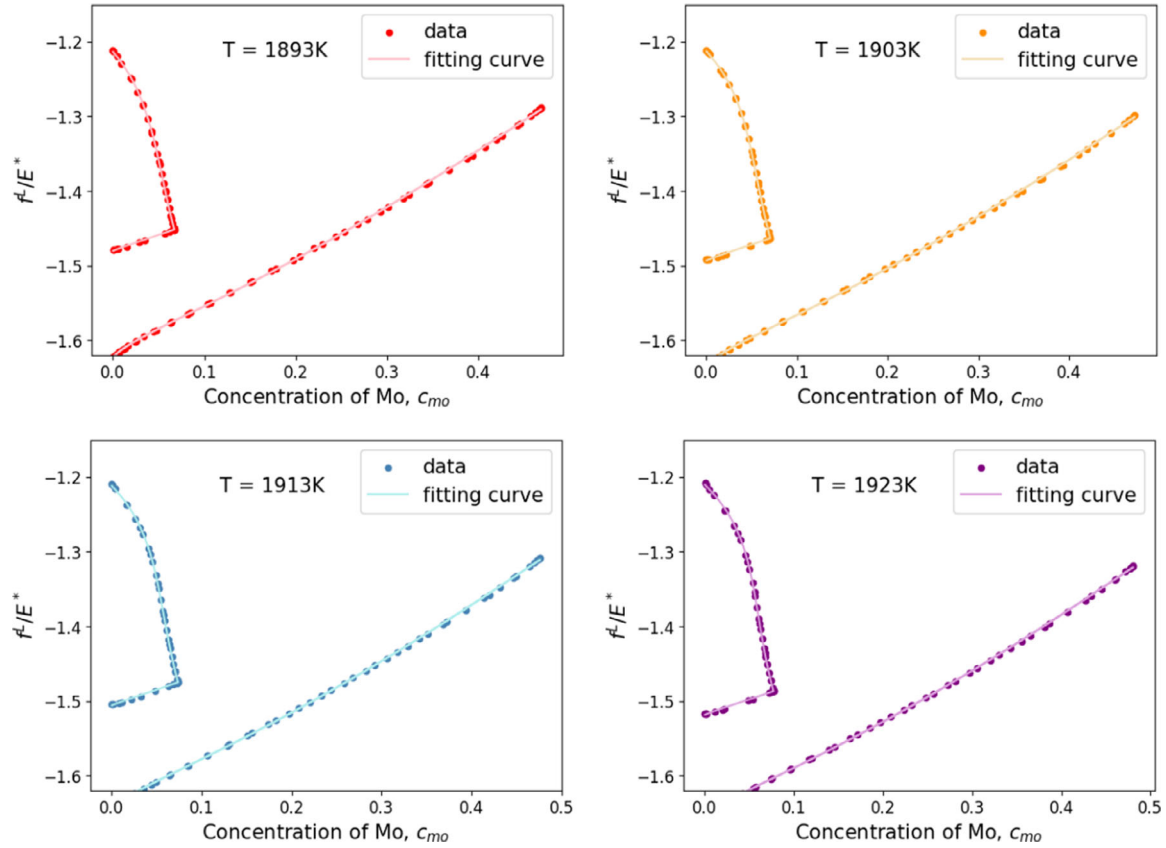


Figure 1. The free energy density of liquid phase as a function of molybdenum concentration for four different temperatures: 1893, 1903, 1913, and 1923 K.

shown in **Figure 2**. A good agreement between the fitted free energy and the CALPHAD dataset reveals the effectiveness of the current fitting method. Moreover, we delineate all coefficients, a , b , d , e , g , h , n , as a function of temperature. To achieve a temperature-dependent description, we expand the coefficients as exemplarily illustrated as follows for the terms incorporated in Equation (6):

$$f^{\text{TS}} = a^{\text{TS}*}(T)c_{\text{Mo}}^{\text{TS}}c_{\text{Mo}}^{\text{TS}} + b^{\text{TS}*}(T)c_{\text{Mo}}^{\text{TS}} + d^{\text{TS}*}(T) + e^{\text{TS}*}(T)c_{\text{Ti}}^{\text{TS}}c_{\text{Ti}}^{\text{TS}} + g^{\text{TS}*}(T)c_{\text{Ti}}^{\text{TS}} + h^{\text{TS}*}(T)c_{\text{Mo}}^{\text{TS}}c_{\text{Ti}}^{\text{TS}} \quad (8)$$

where

$$\begin{aligned} a^{\text{TS}*} &= a^{\text{TS}} + n^{\text{TS}} \\ b^{\text{TS}*} &= 2a^{\text{TS}}b^{\text{TS}} - 1.25n^{\text{TS}} \\ d^{\text{TS}*} &= a^{\text{TS}}b^{\text{TS}2} + d^{\text{TS}} + 0.625^2n^{\text{TS}} \\ e^{\text{TS}*} &= n^{\text{TS}} \\ g^{\text{TS}*} &= -1.25n^{\text{TS}} \\ h^{\text{TS}*} &= 2n^{\text{TS}} \end{aligned} \quad (9)$$

where, every coefficient in the free energy functions is written as a power series of temperature. The temperature dependence of the coefficients is fitted by a linear function and are formulated as

$$\begin{aligned} a^{\text{TS}*}(T) &= 0.279T - 388.9 \\ b^{\text{TS}*}(T) &= -0.348T + 486.8 \\ d^{\text{TS}*}(T) &= 0.108T - 152.3 \\ e^{\text{TS}*}(T) &= 0.278T - 389.1 \\ g^{\text{TS}*}(T) &= -0.348T + 486.4 \\ h^{\text{TS}*}(T) &= 0.556T - 778.3 \end{aligned} \quad (10)$$

All six coefficients in the free energy expression of TS phase as a function of temperature are depicted in **Figure 3**. In the relatively small temperature range from 1893 to 1903 K, the present fitting method via a linear function exhibits a good agreement with CALPHAD database, providing a reliable thermodynamic information for the following phase-field simulations. The relationship between the coefficients in the free energy functions and the temperature for the liquid and β phases is obtained similarly and shown in Appendix to avoid abundance.

Based on these fitted free energy functions, the reconstructed isothermal sections of L-TS- β phase region in Mo-Si-Ti system at temperature 1893, 1898, and 1903 K are shown in **Figure 4a–c**, respectively. The blue, yellow, and red lines correspond to the TS, liquid, and β phases, respectively. The equilibrium concentrations calculated by the fitted free energy functions are illustrated by open circle. The data from CALPHAD database^[25] is represented by full circles for a comparison. As shown in **Figure 4a–c**, at every

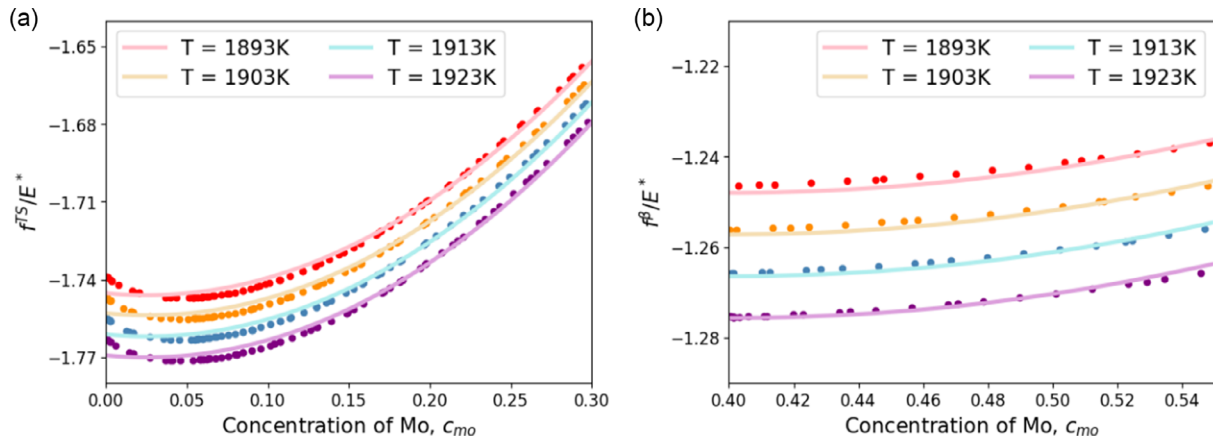


Figure 2. a,b) are the free energy density of TS and MS phases as a function of molybdenum concentration at different temperatures.

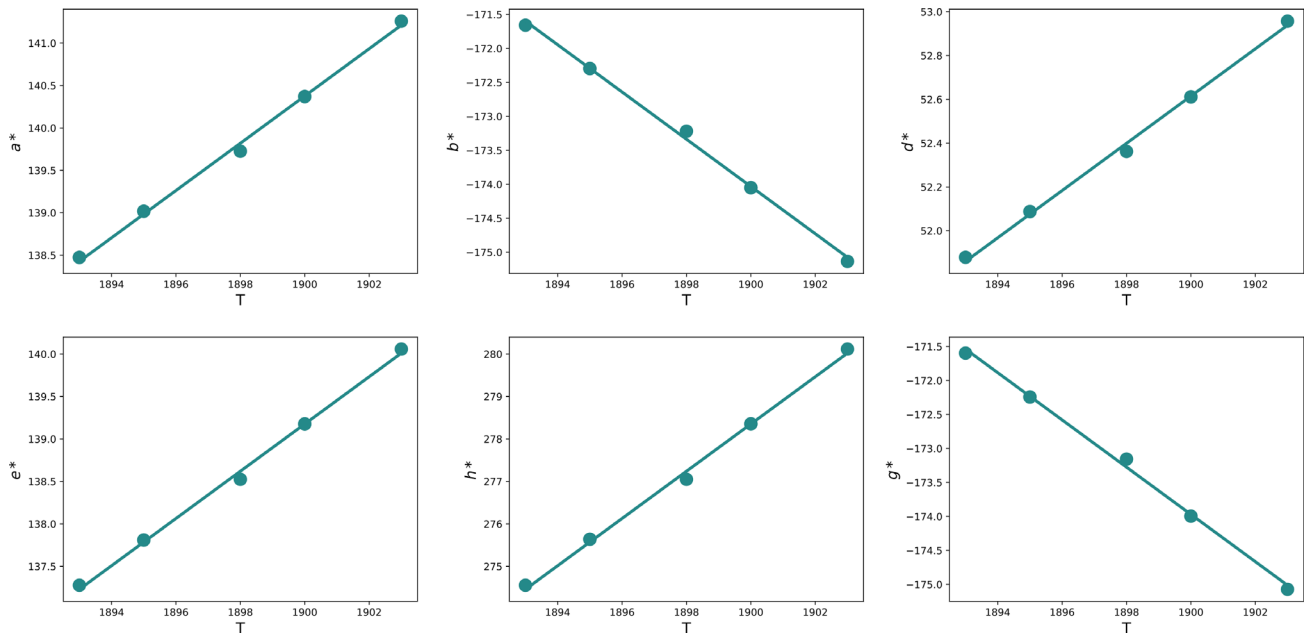


Figure 3. The six coefficients a , b , d , e , g , h in the free energy function of TS phase as a function of temperature.

temperature, the single phase regions of these three phases, which are calculated by the parabolic free energy functions, almost overlap with the ones from CALPHAD. The L-TS- β three phase region is marked by the black triangle, corresponding to the triangle in the isothermal section of Mo-Si-Ti phase diagram at 1893, 1898, and 1903 K, as depicted in Figure 4d–f, respectively. It implies that the present fitted free energy functions can be used in the phase-field simulations to investigate the three-phase eutectic transformation with quantitative input from the CALPHAD database.

4. Results and Discussion

The previous studies of eutectic transformation paid more attention to the lamellar growth after forming the interface between two solid phases. In these considerations, the focus is on the late

state of the nucleation where the solid–solid interface has already been established. However, what happens before the establishment of the solid–solid interface remains an unsolved issue. In particular, the nucleation size and distance are strongly affected by the solidification condition and show relatively large data scattering, as reported in literature. In the present work, we consider the influence of the initial nucleation density and the interfacial energy on the final solidified microstructures. The latter one has been partially addressed in our previous work.^[24] The combined effect of the initial nucleation density and the unequal interfacial energy is investigated in this section.

The multi-PF model is applied to simulate the three-phase eutectic transformation ($L \rightarrow \text{Ti}(\text{Mo})_5\text{Si}_3 + \beta(\text{Mo}, \text{Si}, \text{Ti})$) in Mo-Si-Ti alloy during an isothermal solidification process at the temperature $T_0 = 1893$ K. The zero-gradient Neumann boundary condition for all fields is applied at the solidified end of the

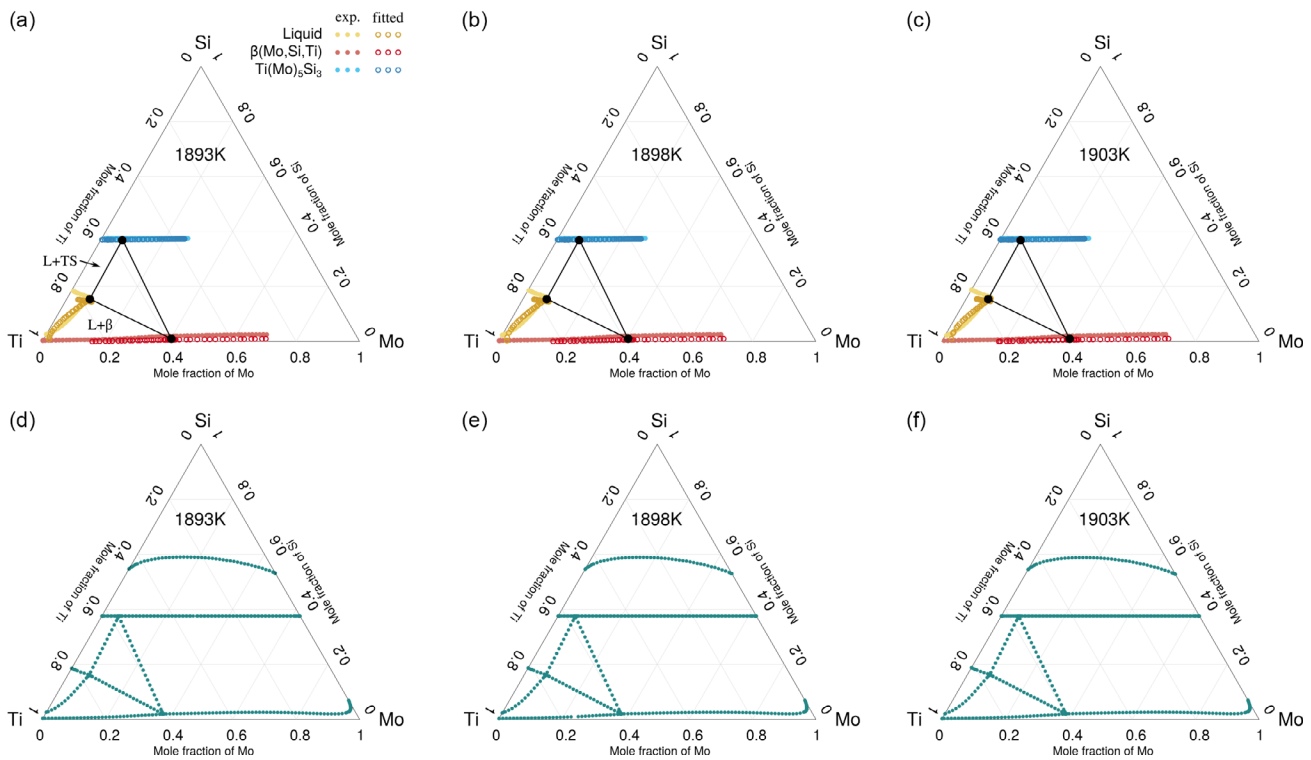


Figure 4. a–c) The reconstructed isothermal sections of L-TS- β phase region in the Mo-Si-Ti system at temperature $T = 1893, 1898,$ and 1903 K. d–f) The isothermal sections of Mo-Si-Ti phase diagram at temperature $T = 1893, 1898,$ and 1903 K based on the thermodynamic database.^[25]

domain. An infinite domain perpendicular to the solidification front is modeled by periodic boundary condition. At the liquid end of the domain, a constant flux of melt is realized by the Dirichlet boundary condition via setting a constant composition $c^L = (c_{\text{Mo}}^L, c_{\text{Ti}}^L, c_{\text{Si}}^L) = (0.073, 0.778, 0.149)$. Considering this infinite flux of melt, the negligible evolution of the solidified phases, and the reduction in the computational effort, we only simulate the region around the solidification front. This is achieved by a moving window technique,^[39] which is controlled by the height of solidification front. As shown in **Figure 5a**, two semicircular nuclei of TS and β phases are filled in the melt of eutectic composition at $T = 1913$ K, which indicates an undercooling of 20 K for the eutectic growth. The nuclei of the two solid phases are set with the same radius of $r = 0.15 \mu\text{m}$, which is larger than the critical nucleation radius (classic nucleation theory) for the case with the greatest interfacial energy and than the interface width of $0.12 \mu\text{m}$ to ensure a stable numerical simulation.

4.1. Nucleation Density and Distance

Due to the nucleation randomness, in general, the distance between a TS nucleus and a β nucleus is not necessarily uniform and may vary in space. In this section, we investigate how the morphological evolution of the lamellar pair is affected by the unequal nucleation distance. The nucleation distance ratio R is defined as

$$R = \frac{D}{S - D - 4r} \quad (11)$$

where D is the distance between TS and β particles and S depicts the domain size, indicating one pair nuclei per unit length (see **Figure 5a**). The nucleation density may be related to the parameter S as $\approx 1/S^d$, where d is the dimension.

The eutectic growth with different nucleation densities is achieved by changing S . By varying S and R , we scrutinize the morphological evolution of the eutectics and observe three different growth modes for the development of eutectics: (g_i) stable, (g_{ii}) regular tilted, and (g_{iii}) irregular growth modes, as shown in **Figure 5**. Here, we consider $R > 1$ due to the mirror-symmetry of the β nuclei with respect to TS particle. For the growth modes, g_{ii} and g_{iii} , we define an orientation angle Φ between the TS/ β interface and x -direction to characterize the tilted growth of the lamellar pair, as depicted in **Figure 5b**; the value of Φ is obtained via calculating the interface tangent. **Figure 5d,e** illustrate the growth of lamellae with varying R (**Figure 5d** for $R = 2.1$ and **Figure 5e** for $R = 4.8$) for a fixed $S = 1.2 \mu\text{m}$. In both figures, the lamellar pairs initially exhibit a slightly bending growth during the eutectic transformation, ultimately returning to a stable growth. For the fixed value $S = 1.2 \mu\text{m}$, the final morphology of eutectics is unaffected by R and always maintains a stable lamellar microstructure. With increasing S to $1.4 \mu\text{m}$, the evolution of the eutectics is depicted in **Figure 5f,g** for $R = 1.7$ and 6.6 , respectively. In this case, we observe lamellae growth with an orientation angle deviating from the x -direction. In this tilted growth mode, the orientation angle Φ is related with R ; its dependence on the nucleation distance ratio will be rationalized later. When S is relatively large ($S = 1.6 \mu\text{m}$), the solidified microstructure of

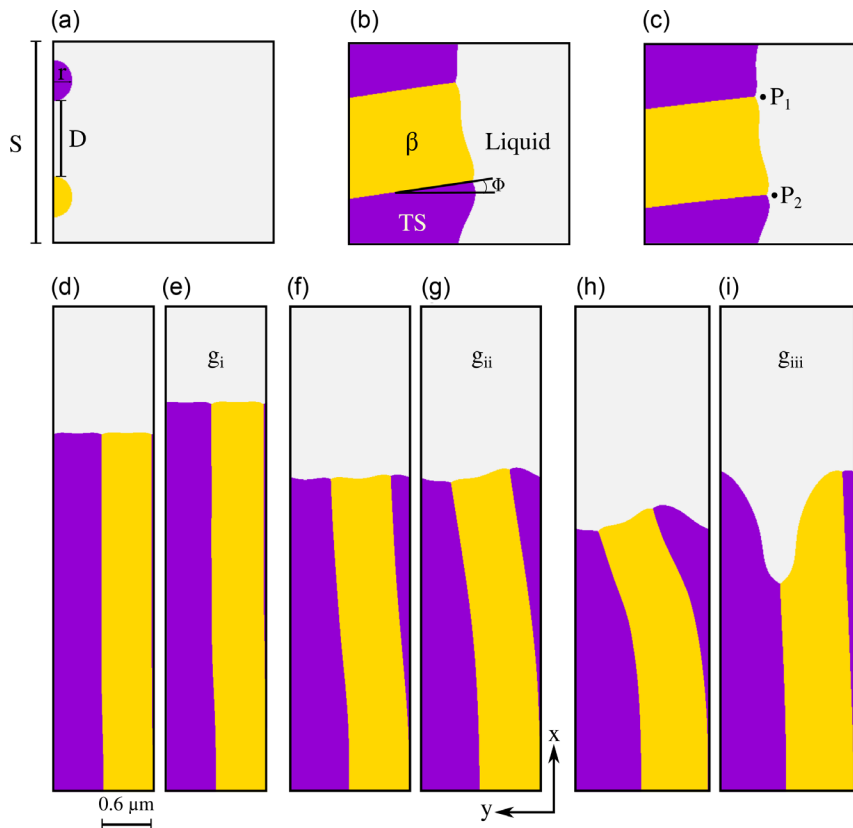


Figure 5. a–c) Schematic illustration of the nucleation distance D , initial seed radius r , domain size S , the orientation angle Φ , and two representative points P_1 and P_2 in melt. The morphological evolution of eutectic lamellae for six cases: d) $R = 2.1$ and $S = 1.2 \mu\text{m}$, e) $R = 4.8$ and $S = 1.2 \mu\text{m}$, f) $R = 1.7$ and $S = 1.4 \mu\text{m}$, g) $R = 6.6$ and $S = 1.4 \mu\text{m}$, h) $R = 2.4$ and $S = 1.6 \mu\text{m}$, i) $R = 13.9$ and $S = 1.6 \mu\text{m}$. Three typical growth modes of eutectic evolution: (g) stable, (g_i) regular tilted, and (g_{iii}) irregular growth modes.

the eutectic lamellae is strongly dependent on the nucleation distance ratio R . For the case with comparable nucleation distance between TS and neighbouring two β particles, namely $R = 2.4$ in Figure 5h, the lamellar pair exhibits a bending growth, whereas an irregular growth mode is observed in the case with $R = 13.9$ corresponding to a significant difference in the nucleation distance (Figure 5i).

The orientation angle Φ , characterizing the tilted growth of lamellae, varies with R for a fixed S . A quantitative representation of the relationship between Φ and R for $S = 1.4 \mu\text{m}$ is presented in Figure 6. For the cases with the same S and under the same undercooling, the orientation angle Φ increases with R . The eutectic transformation occurs in supersaturated melt in an isothermal solidification process, therefore the growth of eutectic lamellae is mainly determined by the diffusion of atoms from melt. The deviation of the concentration in the liquid–solid front from the equilibrium concentration leads to the phase transformation and the eutectic growth. Hence, we use the temporal concentration variation of P_1 and P_2 after forming the TS/ β interface, as shown in Figure 5c, to characterize the motions of two triple points. The points P_1 and P_2 are defined at the position in the liquid phase, which is 7 grid cells away in the x -direction from the triple point $L/\text{TS}/\beta$ on either side of the β phase (see Figure 5c).

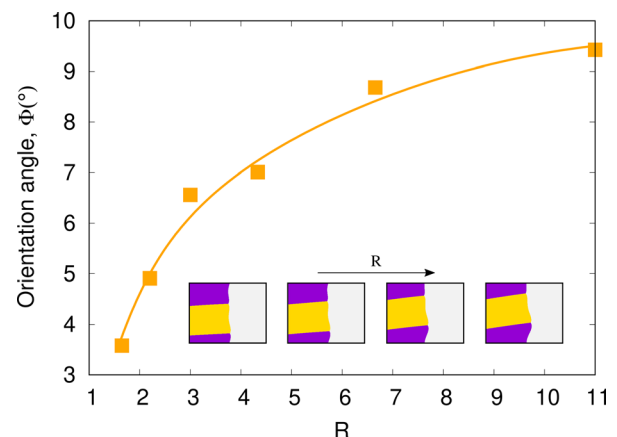


Figure 6. The relationship between the orientation angle Φ and the nucleation distance ratio R .

The corresponding concentration field of molybdenum, silicon, and titanium for three growth modes is illustrated in Figure 7. Mo-rich β phase and Si-rich TS phase grow toward liquid. The titanium content in both solid phases is nearly identical. Next, we analyze the concentration variation of three elements at

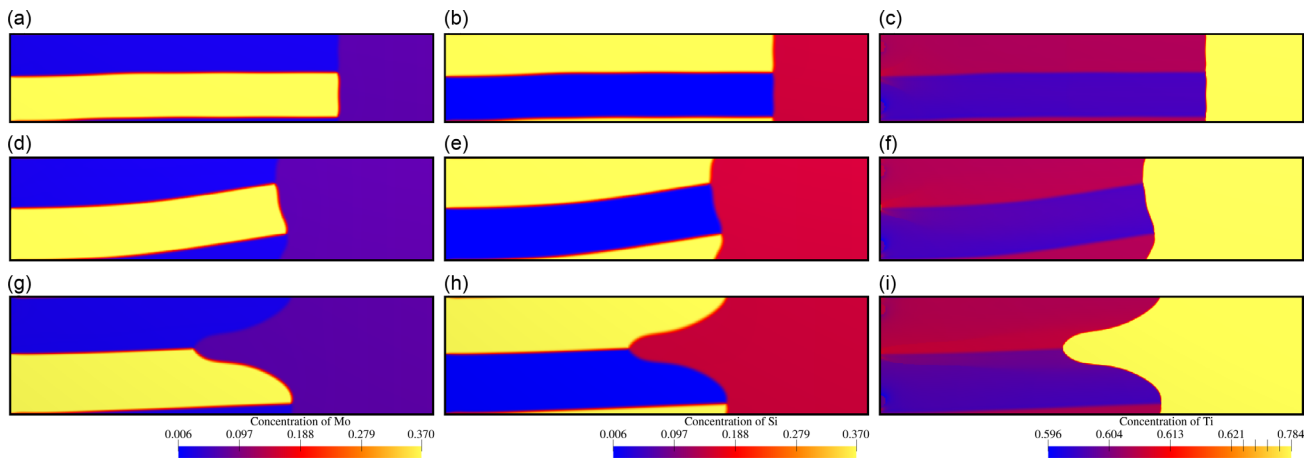


Figure 7. The concentration field of Mo, Si, Ti for three growth modes: a–c) stable growth (type g_i), d–f) regular tilted growth (type g_{ii}), g–i) irregular growth (type g_{iii}).

P_1 and P_2 , defined in Figure 5c, to explain the mechanism for these three distinct growth modes.

Figure 8a–c portray the temporal fluctuations in concentration of molybdenum, silicon, and titanium, respectively, corresponding to the stable growth mode illustrated in Figure 5e. The temporal dependence of three components in the case depicted in Figure 5g for the regular tilted growth is shown in Figure 8d–f. The concentration variation of three elements in the irregular growth mode, as shown in Figure 5i, is depicted in Figure 8g–i. In all figures, the concentration variation at P_1 and P_2 is represented by blue and yellow lines, respectively. Due to the asymmetric nucleation of solid particles ($R \neq 1$), the concentration of the three components significantly differs from each other at these two points in the initial stage in all three cases, leading to an unequal growth velocity of P_1 and P_2 at the beginning of the eutectic transformation. Consequently, the lamellar growth initially exhibits tilted growth in all three growth modes. For the stable growth mode, this initial concentration difference of three components at these two points diminishes over time. As the concentration at these two points becomes equal, the two eutectic phases grow along the x -direction with the same velocity, forming a stable lamellar microstructure. Conversely, the concentration difference persists in the other two growth modes. The concentrations at P_1 and P_2 gradually approach each other over time until reaching a comparable ratio, resulting in the tilted growth with an orientation angle. When the concentration of all components at P_1 and P_2 maintains a significant difference, the growth velocity at these two points is distinctly different, giving rise to the irregular growth mode.

The diffusion process consists of two parts: Along the growth direction called axial diffusion and perpendicular to the growth direction called lateral diffusion. In the present study, the melt composition remains constant indicating negligible difference in axial diffusion. For the lateral diffusion, its diffusion path increases with enlarging S . When the eutectic transformation occurs with a small S , the lateral diffusion is pronounced due to the relatively short diffusion path. As a result of this, the concentration difference at P_1 and P_2 can be compensated by the lateral diffusion, rendering the effect of R negligible. With

increasing S , the concentration difference is difficult to be compensated by the weaker lateral diffusion, giving rise to the tilted growth. In addition, the difference in the concentration increases with $R1$. Therefore, the eutectic growth shows an irregular microstructure observed in the cases with large S and R .

4.2. Interfacial Energy

Owing to the challenge for experimental measurement of the interfacial energies of solid–solid and solid–liquid in Mo–Si–Ti alloy, we systematically investigate the effect of interfacial energies on the morphological evolution of the lamellar pair via modeling and simulation. In this section, we explore the eutectic development under the combined effect of unequal interfacial energy and unequal nucleation distance. The domain size S and the ratio R are set as $1.2 \mu\text{m}$ and 4.8 , respectively, to ensure a stable lamellar microstructure for the fixed supersaturated melt (see Figure 5e). **Figure 9a–f** portrays the morphological evolution of lamellar pair with different angles θ at the triple junction. Here, the angle θ is defined as the one between β -TS interface and liquid-TS interface according to Neumann's triangle rule based on the interfacial energies, $\sigma_{TS/\beta}$, $\sigma_{L/\beta}$, and $\sigma_{L/TS}$ (see Figure 9c). Through changing the interfacial energies $\sigma_{L/\beta}$ and keeping $\sigma_{TS/\beta} = \sigma_{L/TS} = 0.5 \text{ Jm}^{-2}$, the static contact angle θ is manipulated. For an enhanced clarity, the orientation angle Φ is considered positive when the growth of lamellae is anti-clockwise. Conversely, a negative orientation is assigned when the lamellae growth is clockwise. The corresponding concentration field of three components for these six representative cases is illustrated in **Figure 10**. The orientation angles for these six cases are summarized in **Table 3**.

As θ increases, the orientation angle Φ transitions from a positive orientation, through a zero orientation angle, representing stable growth, and ultimately to a negative orientation angle. The supersaturation in melt provides the driving force for the growth of eutectic phases, whereas the capillary force $\sigma\kappa$ prevents it from growth (κ is the surface curvature). The enlargement in θ indicates a decrease in $\sigma_{L/\beta}$. Due to the asymmetric geometry of the

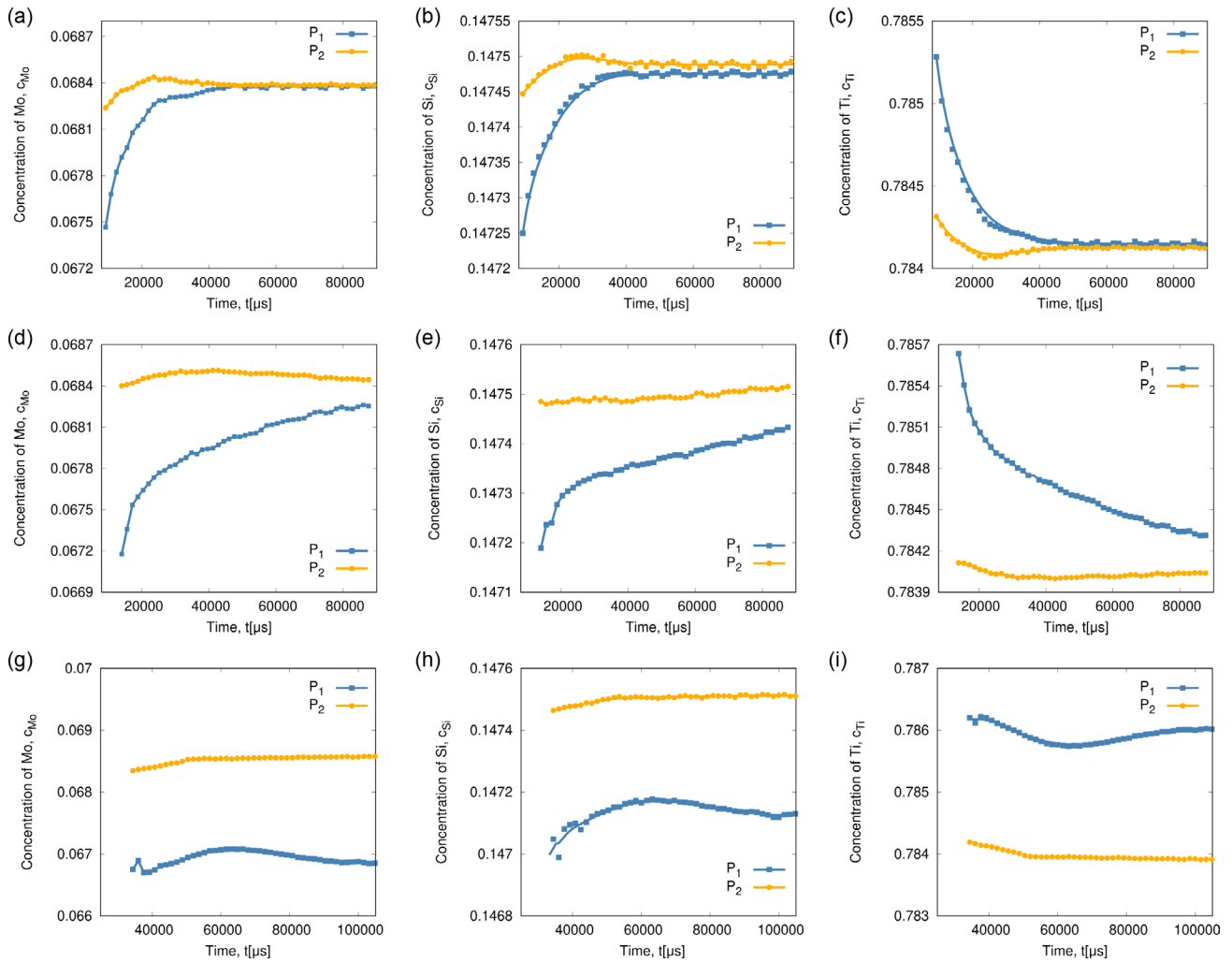


Figure 8. The concentration variation of Mo, Si, and Ti with time at P_1 and P_2 points. a–c): Stable growth. d–f): Regular tilted growth. g–i): Irregular growth.

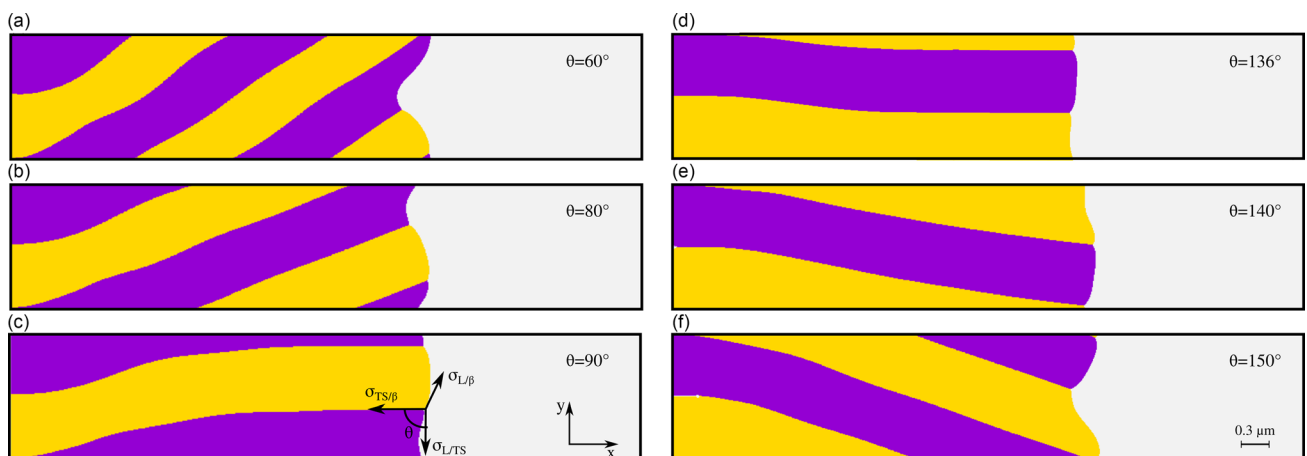


Figure 9. a–f) The solidification morphologies for six representative cases with the contact angle $\theta = 60^\circ, 80^\circ, 90^\circ, 136^\circ, 140^\circ,$ and 150° .

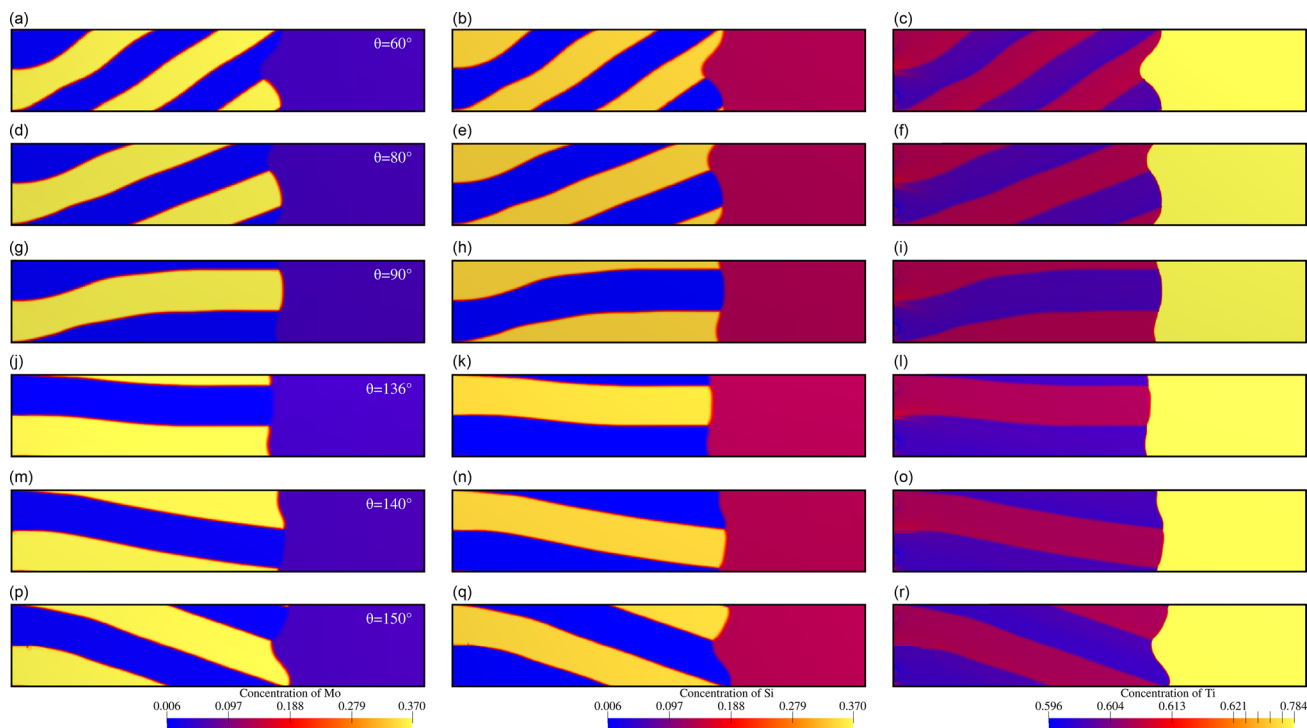


Figure 10. The concentration field of Mo, Si, Ti for the eutectic growth with six contact angles: a–c) $\theta = 60^\circ$, d–f) $\theta = 60^\circ$, g–i) $\theta = 90^\circ$, j–l) $\theta = 136^\circ$, m–o) $\theta = 140^\circ$, and p–r) $\theta = 150^\circ$.

Table 3. The orientation angle for the eutectic growth with different θ .

θ [°]	60	80	90	136	140	150
ϕ [°]	34.9	12.4	0	0	−5.8	−12.5

TS phase on both sides, the capillary force of the β phase is distinct, leading to unequal growth velocities at the two triple points P_1 and P_2 . In this scenario, the growth velocity difference at P_1 and P_2 is influenced by two factors: one arises from the uneven nucleation distance, and the other stems from the disparity in contributions from the capillary force. As the nucleation distance ratio R remains constant, the former effect persists across all cases with different θ . When $\sigma_{L/\beta} > \sigma_{L/TS}$, both effects lead to a similar influence on the difference in the growth velocity. The superimposed effect of these two factors gives rise to a large difference in the growth rate.

With increasing θ , the superimposed effect weakens until $\sigma_{L/\beta} < \sigma_{L/TS}$, at which point these two effects on the growth velocity counterbalance each other. When the latter effect dominates lamellar growth (e.g., for the cases with $\theta = 140$ or 150), a reverse difference in growth velocity emerges.

As discussed in the previous section, if the difference in growth rates can be compensated by lateral diffusion, the lamellar growth exhibits stability. Conversely, when there is an excessive difference in growth velocities, the lamellae display tilted growth. The tilting direction depends on the combined effect of these two factors.

5. Conclusion

In summary, by applying the phase-field model coupling with CALPHAD database, we have studied the formation of the misoriented microstructure in the eutectic solidification process of Mo-Si-Ti alloy. According to previous studies, the nucleation density can vary in a relatively large range in the process of solidification. By setting the nucleation distance and density within the range of previous reports, we show that misoriented eutectic lamellar pairs occur in the process of the solidification. The simulation results demonstrate that the misorientation angle increases with the spacial asymmetry of the nuclei of TS and β . The misorientation angle can be up to 10° caused by the asymmetry of the nucleation distance. The misorientation effect becomes more enhanced when considering unequal interfacial energies of β/L and TS/L. In particular, the misorientation angle is increased to around 35° for the ratio of the interfacial energies, $\sigma_{TS/\beta}/\sigma_{L/TS} = 1.7$, as observed in the present phase-field simulations. We expect that a further increase in the ratio of the solid-liquid interfacial energies and the space asymmetry can lead to a more pronounced misoriented lamellar pair. However, the actual value of the solid-liquid interfacial energies and the spacial distribution of the nuclei rely on a more precise experimental measurement in future works.

Another perspective of the present work is the 3D arrangement of the nuclei. In 3D, there is another spacial freedom to consider the spacial asymmetry of the nuclei; in this case, the orientation angle is not constrained in a 2D plane any more. In a forthcoming work, we will take the 3D nuclei distance in

combination with the unequal interfacial energies into account. Additionally, the influence of the radius and the shape of the initial nuclei in 2D and 3D will be explored in a forthcoming work.

The misoriented microstructure may be affected by the temperature effect when a directional solidification is considered. In contrast to the present isothermal solidification, a temperature gradient can significantly affect the orientation angle. For instance, when a linear temperature gradient is imposed in the domain perpendicular to the solidification front, the lamellar pair tends to grow following the direction of the temperature gradient. In such a case, we expect a diminishing effect of the tilt lamellar pair, which will be addressed in a separate work.

Supporting Information

Supporting Information is available from the Wiley Online Library or from the author.

Acknowledgements

The main part of the research has been carried out through funding by the German Research Foundation (DFG) within the frame of the Research Training group 2561: Materials Compounds from Composite Materials for Applications in Extreme Conditions, which is gratefully acknowledged. Modelling issues to formulate all energy density contributions to the phase-field method as well as the discussion of results have been supported by the VirtMat project P09 Wetting Phenomena of the Helmholtz association (MSE program no. 43.31.02). A special thanks goes to Ms. Jiawen Meng for fitting the thermodynamic data.

Open access funding enabled and organized by Projekt DEAL.

Conflict of Interest

The authors declare no conflict of interest.

Data Availability Statement

The data that support the findings of this study are available from the corresponding author upon reasonable request.

Keywords

eutectic lamellar, misoriented microstructure, nucleation distance and density, phase-field model, solidification of Mo-Si-Ti alloy

Received: December 6, 2023

Revised: March 26, 2024

Published online:

- [1] D. Schliephake, A. Kauffmann, X. Cong, C. Gombola, M. Azim, B. Gorr, H.-J. Christ, M. Heilmaier, *Intermetallics* **2019**, *104*, 133.
- [2] S. Obert, A. Kauffmann, M. Heilmaier, *Acta Mater.* **2020**, *184*, 132.
- [3] S. Obert, A. Kauffmann, S. Seils, S. Schellert, M. Weber, B. Gorr, H.-J. Christ, M. Heilmaier, *J. Mater. Res. Technol.* **2020**, *9*, 8556.
- [4] A. S. Tirunilai, F. Hinrichs, D. Schliephake, M. Engstler, F. Mücklich, S. Obert, G. Winkens, A. Kauffmann, M. Heilmaier, *Adv. Eng. Mater.* **2022**, *24*, 2200918.
- [5] A. Parisi, M. Plapp, *Acta Mater.* **2008**, *56*, 1348.
- [6] V. Podolinsky, Y. Taran, V. Drykin, *J. Cryst. Growth* **1986**, *74*, 57.

- [7] C. Ratsch, J. A. Venables, *J. Vac. Sci. Technol.*, **A 2003**, *21*, S96.
- [8] Y. Gao, B. Wang, J. Huang, T. Gao, W. Yang, Q. Xie, Q. Chen, *Cryst. Growth Des.* **2022**, *22*, 2417.
- [9] A. Durga, P. Wollants, N. Moelans, *Acta Mater.* **2020**, *188*, 241.
- [10] G. Boussinot, M. Döring, S. Hemes, O. Stryzhyboroda, M. Apel, M. Schmidt, *Mater. Des.* **2021**, *198*, 109299.
- [11] J.-H. Kang, J. Park, K. Song, C.-S. Oh, O. Shchyglo, I. Steinbach, *J. Magnesium Alloys* **2022**, *10*, 1672.
- [12] K. Dargahi Noubary, M. Kellner, B. Nestler, *Materials* **2022**, *15*, 3.
- [13] M. Kellner, C. Schulz, A. Kauffmann, M. Heilmaier, B. Nestler, *Crystals* **2023**, *13*, 7.
- [14] Y. Cai, F. Wang, Z. Zhang, B. Nestler, *Acta Mater.* **2021**, *219*, 117223.
- [15] J. Mo, X.-M. Li, L. Luo, B.-B. Peng, *Mater. Res. Express* **2021**, *8*, 036502.
- [16] A. Lahiri, C. Tiwary, K. Chattopadhyay, A. Choudhury, *Comput. Mater. Sci.* **2017**, *130*, 109.
- [17] A. Zhang, J. Du, Z. Guo, S. Xiong, *Phys. Rev. E* **2018**, *98*, 043301.
- [18] V. P. Laxmipathy, F. Wang, M. Selzer, B. Nestler, *Acta Mater.* **2021**, *204*, 116497.
- [19] V. P. Laxmipathy, F. Wang, M. Selzer, B. Nestler, *Comput. Mater. Sci.* **2021**, *186*, 109964.
- [20] K. Dargahi Noubary, M. Kellner, P. Steinmetz, J. Hötzer, B. Nestler, *Comput. Mater. Sci.* **2017**, *138*, 403.
- [21] M. Plapp, *Phys. Rev. E* **2011**, *84*, 031601.
- [22] A. Choudhury, B. Nestler, *Phys. Rev. E* **2012**, *85*, 021602.
- [23] F. Wang, A. Choudhury, C. Strassacker, B. Nestler, *J. Chem. Phys.* **2012**, *137*, 3.
- [24] Y. Cai, F. Wang, A. Czerny, H. J. Seifert, B. Nestler, *Acta Mater.* **2023**, *258*, 119178.
- [25] Y. Yang, Y. Chang, L. Tan, W. Cao, *Acta Mater.* **2005**, *53*, 1711.
- [26] A. Karma, *Phys. Rev. Lett.* **2001**, *87*, 115701.
- [27] N. Moelans, *Acta Mater.* **2011**, *59*, 1077.
- [28] F. Wang, B. Nestler, *Acta Mater.* **2015**, *95*, 65.
- [29] Q.-L. Cao, D.-H. Huang, J.-S. Yang, M.-J. Wan, F.-H. Wang, *Chin. Phys. Lett.* **2014**, *31*, 66202.
- [30] Y. Cai, F. Wang, M. Selzer, B. Nestler, *Modell. Simul. Mater. Sci. Eng.* **2019**, *27*, 065010.
- [31] H. Mehrer, *Mater. Trans., JIM* **1996**, *37*, 1259.
- [32] X. Wu, J. Zhong, L. Zhang, *Acta Mater.* **2020**, *188*, 665.
- [33] M. A. Dayananda, Y. H. Sohn, *Metall. Mater. Trans. A* **1999**, *30*, 535.
- [34] Y. Liu, W.-F. Wei, K.-C. Zhou, L.-F. Chen, H.-P. Tang, *J. Cent. South Univ. Technol.* **2003**, *10*, 81.
- [35] N. E. Singh-Miller, N. Marzari, *Phys. Rev. B* **2009**, *80*, 235407.
- [36] N. G. Hörmann, N. Marzari, K. Reuter, *npj Comput. Mater.* **2020**, *6*, 136.
- [37] F. Wang, B. Nestler, *Phys. Rev. Lett.* **2024**, *132*, 126202.
- [38] F. Wang, P. Altschuh, A. M. Matz, J. Heimann, B. S. Matz, B. Nestler, N. Jost, *Acta Mater.* **2019**, *170*, 138.
- [39] A. Vondrous, M. Selzer, J. Hötzer, B. Nestler, *Int. J. High Perform. Comput. Appl.* **2014**, *28*, 61.
- [40] E. Sukeidai, M. Shimoda, H. Nishizawa, Y. Nako, *Mater. Trans.* **2011**, *52*, 324.
- [41] J. Perepezko, R. Hebert, R. Wu, G. Wilde, *J. Non-Cryst. Solids* **2003**, *317*, 52, advances in Metallic Glasses.
- [42] H. Chen, Y. He, G. Shiflet, S. Poon, *Scr. Metall. Mater.* **1991**, *25*, 1421.
- [43] D. Allen, J. Foley, J. Perepezko, *Acta Mater.* **1998**, *46*, 431.
- [44] G. Wilde, H. Sieber, J. Perepezko, *Scr. Mater.* **1999**, *40*, 779.
- [45] C. Puncreobutr, A. Phillion, J. Fife, P. Rockett, A. Horsfield, P. Lee, *Acta Mater.* **2014**, *79*, 292.
- [46] A. M. Macner, S. Daniel, P. H. Steen, *Langmuir* **2014**, *30*, 1788, pMID: 24490757.
- [47] C.-W. Lo, C.-C. Wang, M.-C. Lu, *Adv. Funct. Mater.* **2014**, *24*, 1211.
- [48] H. Cha, H. Vahabi, A. Wu, S. Chavan, M.-K. Kim, S. Sett, S. A. Bosch, W. Wang, A. K. Kota, N. Miljkovic, *Sci. Adv.* **2020**, *6*, eaax0746.